Average Cell Orientation, Shape and Size Estimated from Tissue Images

Peter J.W. Iles, David A. Clausi, Shannon M. Puddister and G. Wayne Brodland
Dept. of Systems Design Engineering, University of Waterloo, Waterloo, ON, Canada, N2L 3G1
{pjwiles, dclausi, brodland}@uwaterloo.ca, spuddister@gmail.com

***Abstract*— Four computer vision algorithms to measure the average orientation, shape and size of cells in images of biological tissue are proposed and tested. These properties, which can be embodied by an elliptical 'composite cell' are crucial for biomechanical tissue models. To automatically determine these properties is challenging due to the diverse nature of the image data, with tremendous and unpredictable variability in illumination, cell pigmentation, cell shape and cell boundary visibility. First, a simple edge detection routine is performed on the raw images to locate cell edges and remove pigmentation variation. The edge map is then converted into the magnitude spatial-frequency domain where the spatial patterns of the cells appear as energy impulses. Four candidate methods that analyze the spatial-frequency data to estimate the properties of the composite cell are presented and compared. These methods are: Least Squares Ellipse Fitting, Correlation, Area Moments and Gabor Filters. Robustness is demonstrated by successful application on a wide variety of real images.**

***Index Terms*— composite cell, average cell, shape detection, geometry, texture, orientation, aspect ratio, spatial-frequency, embryology, morphogenesis, tissue mechanics, microscopy**

I. Introduction

THIS paper addresses a novel computer vision problem: to estimate the average orientation, shape and size of cells in an image of biological tissue (Fig. 1). These features can be represented by an elliptical 'composite cell' as introduced by Brodland and Veldhuis [1]. This composite cell is defined by its orientation α from the horizontal and major and minor axes L_{major} and L_{minor}, respectively (Fig. 2). The aspect ratio κ and the area A of the ellipse correspond to the shape and size of the composite cell and can be calculated from the axis lengths:

$$\kappa = \frac{L_{major}}{L_{minor}}. \tag{1a}$$

$$A = \frac{\pi}{4} L_{major} L_{minor}. \tag{1b}$$

The objective of the present work is to develop an algorithm that can estimate α, κ and A and is robust to unpredictable image characteristics. This paper proposes four different algorithms that estimate these properties from the spatial-frequency domain data. The methods are compared through application to a wide variety of real images.

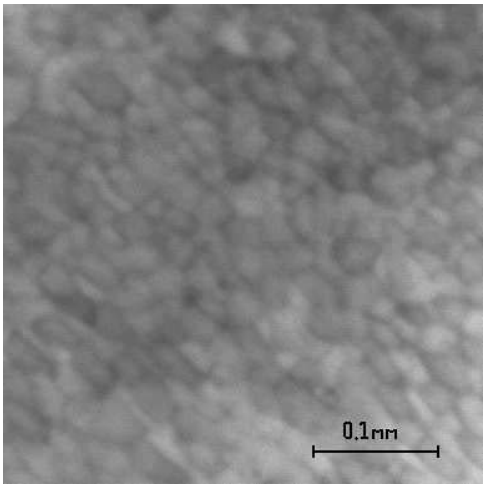

Fig. 1. An image of an embryonic epithelium.

Section II provides background information on this research, which includes a description of the project context, related research and an explanation of how the the composite cell properties can be estimated from spatial-frequency data. The four proposed algorithms are described in Section III, followed by experimental results in Section IV. Conclusions are made in Section V.

II. Background

A. Project Context

This research is in support of biomechanical modelling of embryonic development [2], the purpose of which is to understand the mechanics of embryogenesis and the mechanical basis of birth defects such as spina bifida and cardiac septum defects. Slight irregularities in the stresses occurring in the embryonic epithelia, of which embryos are largely composed, are believed to cause these conditions. It has been shown that these stresses are related to the orientation, shape and size of the epithelium cells as characterized by α, κ and A respectively [3]. Thus, to understand embryo development, it is crucial to measure these properties.

Proceedings of the Second Canadian Conference on Computer and Robot Vision (CRV'05)
0-7695-2319-6/05 $ 20.00 **IEEE**

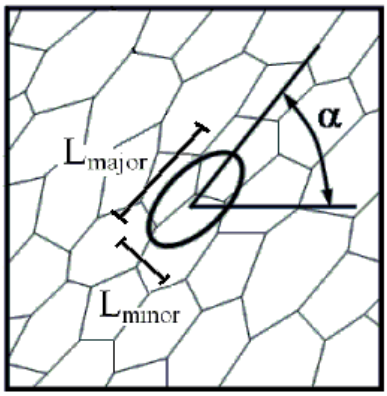

Fig. 2. The composite cell is defined by its orientation α and its major and minor axes, L_{major} and L_{minor}.

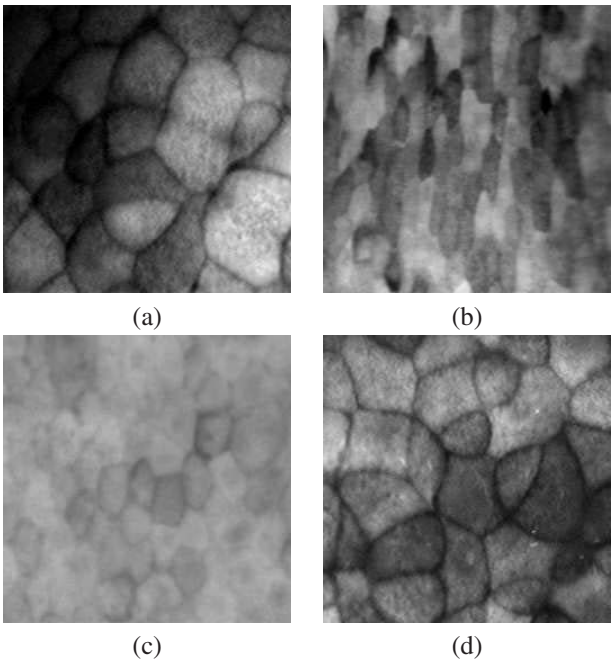

Fig. 3. Variation in image characteristics: (a) illumination, (b) cell pigmentation, (c) cell boundary visibility and (d) cell shape and orientation.

The tissue images considered in this paper were taken from intact developing axolotl (amphibian) embryos using a custom microscope setup [4] and from excised pieces of embryonic tissue placed in a novel instrument that can apply a tensile stress to them [5]. The characteristics of the images make it difficult to design a robust algorithm, primarily due to variability of the image characteristics. Substantial variability is found in illumination, cell pigmentation, cell boundary visibility and cell orientation and shape (Fig. 3). Finally, cell mitosis can cause dark spots to appear between newly forming cells, which can be mistaken as individual cells. An algorithm that is insensitive to these variations is desired.

The need to automate this process rather than relying on human measurement is two-fold. First, the large number of images that must be analyzed makes human measurement impractical. Second, avoiding human bias is preferred, and this can only be guaranteed with an automated method.

B. Related Research

To the best of the authors' knowledge, the specific problem considered in this paper has not been addressed in the research literature. However, the problem is related to texture analysis. The embryonic tissue can be thought of as a texture, having a certain average orientation and 'texture element' shape and size. The primary drawback of the existing methods discussed below is that they are applied only to simple texture images containing very regular lattice structures.

For measuring texture orientation, Vaidyanathan and Lynch analyzed the directionality of detected edges [6]. Sourice et al. proposed computing autocorrelation of pixel intensities to find texture orientation [7]. These methods were tested only on images containing roughly parallel lines, and hence are not appropriate for complex cellular images. Others have focused on computing texture orientation by exploiting patterns in the spatial-frequency domain. These techniques are based on the concept that the power spectrum energy is concentrated along an axis perpendicular to the texture orientation. Bigün et al. [8] propose a method to find an axis of symmetry in the power spectrum in order to estimate orientation while Kass and Witkin [9] use an orientation-selective bandpass filter and find the orientation yielding the greatest response. These methods were also only tested on simple images containing parallel lines.

Also relevant is the body of research on the structural analysis of texture. These methods attempt to detect regularly occurring texture elements arranged according to a 'placement rule'. The placement rule consists of two dominant orientations with corresponding frequencies (Fig. 4). Matsuyama et al. automatically find the placement rule through analysis of the spatial-frequency domain [10] while others use co-occurrence matrix features to perform this task [11] [12]. There are three issues with these methods. First, they are meant for use with simple, regularly repeating texture images (as in Fig. 4a). The embryonic tissue images do not match this description, since they can have large variations in cell size and placement. Second, the embryonic cells are tightly packed which makes it impossible to isolate a single cell in a parallelogram-shaped window (as in Fig. 4b). Finally, here it is desired that the orientation of the cells themselves be detected, rather than the orientation of the *placement pattern* of the cells. The vertical orientation of the elements in Fig. 4a is not captured in the given placement rule. While a placement rule could be used to find κ and A, these algorithms are not suited to the embryonic tissue images.

A previous attempt was made by the authors to estimate the parameters of the composite cell [14], using a novel contrast enhancement method and a watershed segmentation algorithm

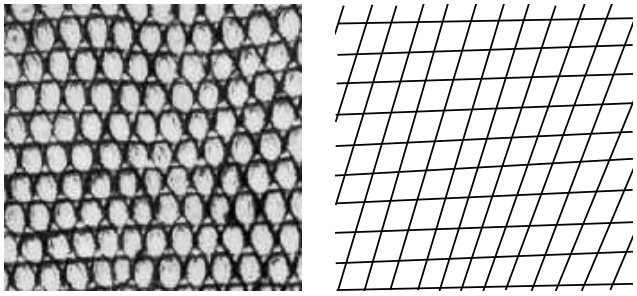

(a) (b)

Fig. 4. Placement rule defining texture element positions. (a) Regularly-repeating texture image [13]. (b) Placement rule grid lines defined by two orientations and two frequencies.

to individually identify the cells. The values of θ, κ and A were found by averaging over all the detected cell segments. Unfortunately, this approach was not sufficiently robust to be widely applicable on embryonic tissue images. Variation in cell edge visibility within images made the selection of contrast enhancement and segmentation thresholds very difficult.

Since none of these algorithms can reliably estimate α, κ and A, algorithms that use only spatial-frequency magnitude information are proposed.

C. Patterns in the Spatial-Frequency Domain

An image is converted into the spatial-frequency domain using a two-dimensional fast Fourier transform (FFT). The magnitude response image ($|F|$) can then be plotted on horizontal *u* and vertical *v* axes, in pixel units of cycles per image (c.p.i.) with the origin of $|F|$ shifted to the center of the image to follow convention.

To illustrate how composite cell properties can be measured in the spatial-frequency domain, first consider the synthetic (Voronoi tessellation) cell image (Fig. 5a) [15] and its corresponding $|F|$ image (Fig. 5b). Note the obvious elliptical shape of the energy distribution.

The necessary information can be derived from an ellipse to fit to the energy distribution in $|F|$. The strong high-frequency response shown in the vertical direction (along the v axis) in the $|F|$ image corresponds to L_{minor} and can be seen visually in the spatial domain as the high density of cell edges encountered in the vertical direction. The relatively weaker low-frequency response in the horizontal direction (along the u axis) corresponds to L_{major}, and can be seen in the spatial domain as the lower density of cell edge encountered in the horizontal direction. It is important to note that the strongest response in the $|F|$ image corresponds to L_{minor} because the number of repetitions of the minor axis in the image is greater than that of the major axis. The orientation, α, is simply perpendicular to the major orientation of the ellipse in the $|F|$ image. The axis lengths of the ellipse in the $|F|$ image can be easily converted from c.p.i. to pixels, allowing κ and A to be calculated using Eq. (1a) and (1b) respectively.

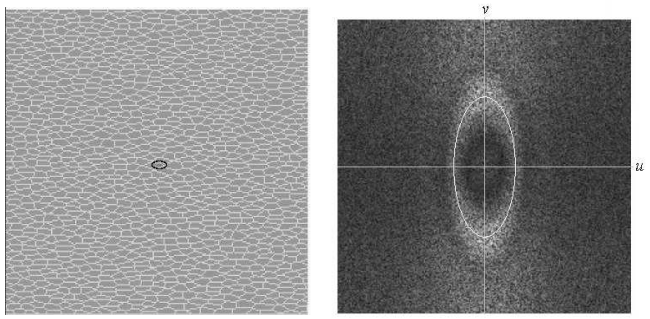

(a) (b)

Fig. 5. A cellular image and its corresponding Fourier transform. (a) A synthetic 350x350 cellular image with $\alpha = 0°$, $\kappa = 1.8$, $A = 24$. The composite cell is drawn in black. (b) Corresponding magnitude response ($|F|$) image in pixel units of cycles per image. Transform of composite cell is shown as white ellipse. A square root point operator has been applied to enhance visibility.

The benefit of using the spatial-frequency domain is that the FFT has the effect of averaging spatial variation. In context of this research, the variations in cell shape and orientation as well as in cell edge visibility are averaged. The other image characteristic issues, illumination and pigmentation variation are addressed in the preprocessing method outlined in the next section.

The difficulty in using a spatial-frequency approach is achieving an accurate fit of an ellipse to the $|F|$ energy distribution. As shown in the next section, images of real axolotl embryonic epithelia do not typically produce $|F|$ images as clean as that shown in Fig. 5b. Four methods to achieve this ellipse fitting are presented.

Stationarity of the geometric parameters of interest is assumed. If these cellular properties vary from location to location, this would create multiple patterns in the spatial-frequency domain, which would not be appropriate data for the proposed methods.

III. Methods

Three preprocessing steps ameliorate the problematic image characteristics.

1) *Perform edge detection*: This is performed on the spatial domain image to detect cell boundaries and remove the effect of cell pigmentation. The authors used the magnitude of the combined horizontal and vertical Sobel operators [16] but any other fundamental edge detector could be used. The FFT is applied to this image.
2) *Set low-frequency components to zero*: Frequencies components at or below 4 cycles per image are set to zero since these components represent spatial patterns too large to be individual cells. The image data will not be captured at such cell resolutions. This also removes low-frequency illumination variation.

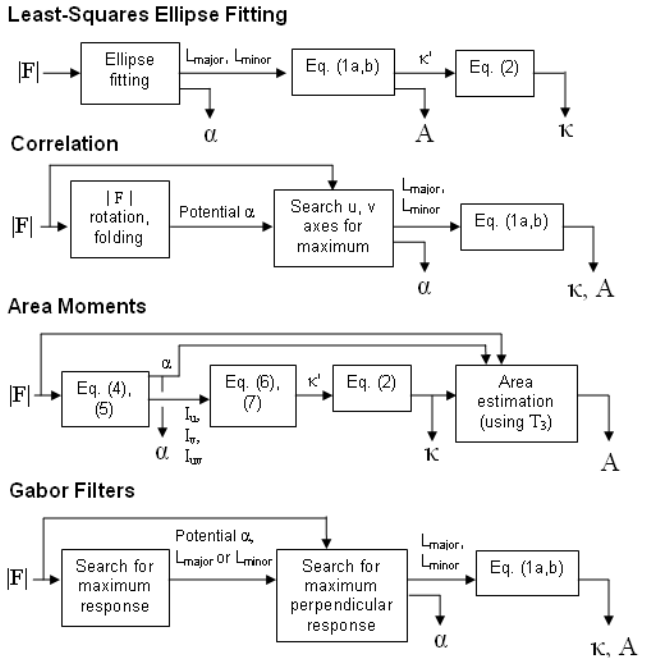

Fig. 6. Summary of methods for finding composite cell parameters α, κ and A from the $|F|$ image.

3) *Threshold* $|F|$: The $|F|$ image is thresholded by setting to zero components below $T_1 = 0.30$ (on a 0-1 scale), in order to remove low-energy noise.

Four methods have been developed to determine the parameters of an ellipse that is fit to the $|F|$ energy distribution. These are: Least Squares Ellipse Fitting, Correlation, Area Moments and Gabor Filters. A summary of how the composite cell parameters are found for each method is shown (Fig. 6).

A. Least-Squares Ellipse Fitting

A direct way to fit an ellipse to the $|F|$ image data is to find the best-fit ellipse in a least-squares sense. Numerous methods have been developed for fitting ellipses to data points. Many of these techniques fit data points to a general conic section and impose an additional constraint to force the solution into an ellipse. Fitzgibbon et al. present a direct least squares based ellipse specific method that is robust and computationally inexpensive [17]. This algorithm is applied to the $|F|$ image.

The $|F|$ image data is converted into a set of data points in the following manner: a data point at pixel column *x* and row *y* is created for each 0.1 pixel intensity value. Thus a pixel with an intensity of 0.4 would be converted into four data points. Such a bin value was chosen to create sufficient points to characterize the $|F|$ image. Once the ellipse is fit to this data, α, L_{major} and L_{minor} can be calculated directly, and κ and A can then be calculated using Eqs. (1a) and (1b).

This values of κ were biased high for this algorithm. This is because the energy corresponding to L_{minor} in the $|F|$ image was larger than that corresponding to L_{major}. The fitted ellipse would therefore consistently be 'stretched' in the L_{minor} direction, resulting in a greater κ value. A linear corrector function was empirically determined (using test images) that minimized the least-squared error of κ:

$$\kappa = \kappa' - T_2(\kappa' - 1) \tag{2}$$

where $T_2 = 0.33$ and κ' is the biased estimate of the true κ. Note that this function does not adjust $\kappa' = 1$, since the aforementioned bias would not have an effect in this case as $L_{minor} = L_{major}$.

B. Area Moments

Area moments provide a measure of the resistance of an object to angular acceleration about an axis. The ellipse in $|F|$ can be thought of as a two-dimensional object of varying density (pixel intensities) centered at the origin. The idea of using area moments in the $|F|$ image to find texture *orientation* was suggested by Bigün et al. [8]; their method actually solves a matrix eigenvalue problem in the spatial domain.

It is proposed that this concept be implemented completely in the magnitude spatial-frequency domain where all three composite cell parameters can be determined. First, the moments about the u and v axes (I_u, I_v) and product of inertia (I_{uv}) of the $|F|$ image can be found as follows [19]:

$$I_u = \sum_{v=1}^{rows} \sum_{u=1}^{cols} |F| \cdot v^2 \tag{3a}$$

$$I_v = \sum_{v=1}^{rows} \sum_{u=1}^{cols} |F| \cdot u^2 \tag{3b}$$

$$I_{uv} = \sum_{v=1}^{rows} \sum_{u=1}^{cols} |F| \cdot u \cdot v \tag{3c}$$

After computing these inertial measures, α can be computed as:

$$\alpha = \arctan\left(\frac{2I_{uv}}{I_u - I_v}\right) \tag{4a}$$

provided $I_u \neq I_v$. In the case that $I_u = I_v$,

$$\alpha = \begin{cases} \pi/4 & \text{if } I_{uv} > 0 \\ 0 & \text{if } I_{uv} = 0 \\ -\pi/4 & \text{if } I_{uv} < 0 \end{cases} \tag{4b}$$

Using Mohr's circle [19], $|F|$ can be rotated by α to set I_{uv} to zero, resulting in only two moments:

$$I_1 = \frac{I_u + I_v}{2} + \sqrt{\left(\frac{I_u - I_v}{2}\right)^2 + I_{uv}^2} \tag{5a}$$

$$I_2 = I_u + I_v - I_1 \tag{5b}$$

κ can then be calculated directly as a ratio of the roots of these moments [20] using:

$$\kappa = \frac{max(\sqrt{I_2}, \sqrt{I_1})}{min(\sqrt{I_2}, \sqrt{I_1})}. \quad (6)$$

As with the LSEF method, the κ values for this method were biased high. The corrector function in Eq. (2) is applied again here.

To estimate A, an ellipse constrained to the estimated α and κ was found that contained a certain fraction T_3 of the energy in the $|F|$ image. The fraction was empirically found to be $T_3 = 0.28$. An ellipse constrained to the estimated α and κ that minimized a least squares distance to the data points was also attempted. This, however, gave inferior results and is mentioned briefly in the results section.

C. Correlation

The third approach uses the correlation coefficient to find orientation. The axis lengths are found by searching for maxima along two rays in the $|F|$ image: one parallel and one perpendicular to the detected orientation.

This correlation coefficient, $-1 < \rho < 1$, is defined for two data vectors, a and b as:

$$\rho = \frac{E[(a - \mu_a)(b - \mu_b)]}{\sqrt{var(a)var(b)}} \quad (7)$$

where $E[.]$ is the expectation operator and $var(.)$ is the sample variance operator. The sample means for a and b are μ_a and μ_b respectively. New images are created by incrementally rotating $|F|$ through $1^\circ < \alpha < 90^\circ$. After each rotation, the image is "folded" along the vertical v axis, and ρ is measured between corresponding pixel intensities using Eq. 7. This is done by arranging the pixels in the left and right halves of the image into vectors a and b respectively. When the $|F|$ ellipse is aligned (either horizontally or vertically) with the u and v axes, ρ is at a maximum (Fig. 7). The angle of rotation used to produce the maximum ρ corresponds to the orientation of either L_{major} or L_{minor}.

The maximum responses along the u and v axes are now found. A narrow 3-pixel-wide band along each axis is considered to account for any small errors in the orientation estimation. Of the two detected maxima, the response found at the higher frequency corresponds to L_{minor} while the response found at the lower frequency corresponds to L_{major}. Gaussian smoothing with $\sigma = 1$ is applied along the narrow bands to minimize the effect of noise. Now α is known and κ and A can be calculated from the measured axis lengths using Eqs. (1a) and (1b).

D. Gabor Filters

Gabor filters are a class of multi-channel filters capable of decomposing an image into a collection of frequency and orientation texture features using multiple resolution techniques

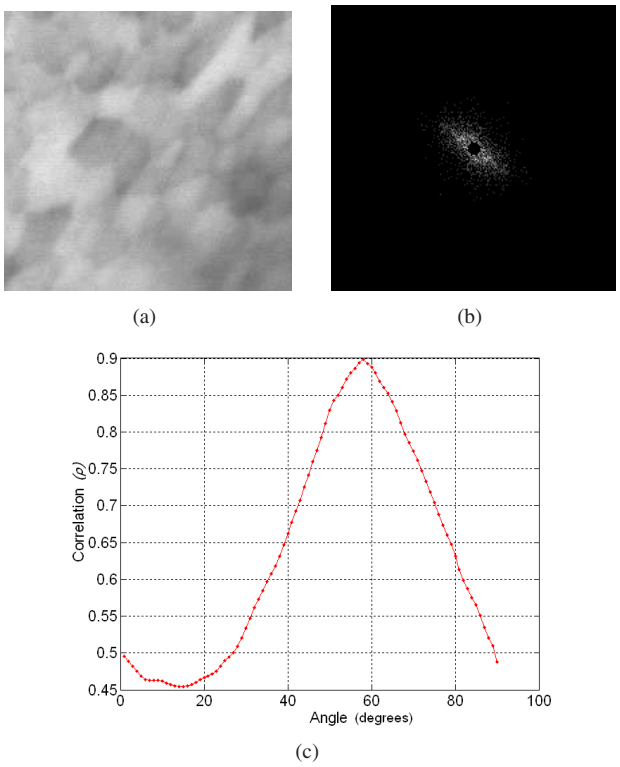

Fig. 7. Estimating orientation using Correlation. (a) Input image with cells rotated at 60° to the horizontal; (b) corresponding preprocessed $|F|$ image; (c) ρ vs. angular rotation shows a well-defined maximum at 60°. This angle corresponds to the orientation of either L_{major} or L_{minor}.

[21] [22]. This means that a Gabor filter can be designed to be sensitive to specific frequencies and orientations. This is in contrast to the orientation-selective filters proposed by Kass and Witkin that can be tuned to specific *orientations* only [9].

The magnitude response of Gabor filters serves as the basis for this algorithm, which searches for the filter parameters that produces the strongest magnitude response in the $|F|$ image. In this framework, filter responses are tested at every second whole value of frequency in the range $min_{Freq} \leq F \leq max_{Freq}$, and every third whole valued orientation in the range $-90^\circ < \alpha \leq 90^\circ$, where min_{Freq} and max_{Freq} are dependent upon the image size and chosen to ensure sufficient coverage of the filter in the search space.

The frequency and orientation of the Gabor filter that produces the strongest magnitude response will be associated with the orientation and axis length of either L_{major} or L_{minor}. A ray perpendicular to this axis is then searched to find the frequency that produces the strongest response. This corresponds to the other axis length of the composite cell. The axes with the higher and lower frequencies become L_{minor} and L_{major}, respectively. The orientation is then associated with L_{major}. As before, κ and A can then be found using Eqs. (1a) and (1b).

Gabor filters were found to be satisfactory only for very

regular celluar images with very strong patterns in the $|F|$ energy distribution [18]. They did not work well for typical cell images and hence are not included in the following section. The maximum Gabor filter responses were consistently being 'pulled' to frequencies that were too high, apparently because of the larger filter bandwidth associated with the higher frequency Gabor filters when implemented using a pseudo-wavelet format [22].

IV. Experimental Results

Ten images of real embryonic epithelia were used to test the Least-Squares Ellipse Fitting (LSEF), Area Moments (AM) and Correlation (CORR) algorithms (Fig. 8). These images were chosen because they demonstrate a wide variety of image characteristics. The corresponding preprocessed $|F|$ images are also shown (Fig. 9).

Tables I-III compare the results of the three methods. The 'true' α, κ and A ($\hat{\alpha}$, $\hat{\kappa}$ and $\hat{A}$ respectively) shown in the leftmost column of each table were calculated by hand-segmenting the test images. For $\hat{\alpha}$ and $\hat{\kappa}$, the average I_u, I_v and I_{uv} were calculated over all cells and Eqs. (3)-(6) were applied. Note that $\hat{\kappa}$ is therefore the average cell aspect ratio *in the direction of* $\hat{\alpha}$. For $\hat{A}$, the cell areas were simply averaged. Only the cells with completely visible boundaries were hand-segmented. This method was validated by applying it to Voronoi tessellations with known $\hat{\alpha}$, $\hat{\kappa}$ and $\hat{A}$ values, and comparing these values to the measured ones. It is understood that hand-segmenting the images results in only the best *estimate* of $\hat{\alpha}$, $\hat{\kappa}$ and A. Standard deviations of $\hat{\alpha}$, $\hat{\kappa}$ and $\hat{A}$ over all cells ($\sigma_{\hat{\alpha}}$, $\sigma_{\hat{\kappa}}$ and $\sigma_{\hat{A}}$ respectively) are also shown in the leftmost column of the tables. It was expected that if $\sigma_{\hat{\alpha}}$, $\sigma_{\hat{\kappa}}$or $\sigma_{\hat{A}}$ were large, then the performance of the algorithms would be degraded.

The distance of the measured α from $\hat{\alpha}$ is measured in degrees ($\epsilon_\alpha = \alpha - \hat{\alpha}$) and number of true standard deviations ($\zeta_\alpha = \epsilon_\alpha / \sigma_{\hat{\alpha}}$). The distance of the measured κ from $\hat{\kappa}$ is measured in dimensionless units ($\epsilon_\kappa = \kappa - \hat{\kappa}$) and also in number of true standard deviations ($\zeta_\kappa = \epsilon_\kappa / \sigma_{\hat{\kappa}}$). Finally, the distance of the measured A from $\hat{A}$ is measured in square pixels ($\epsilon_A = A - \hat{A}$) and also in number of true standard deviations ($\zeta_A = \epsilon_A / \sigma_{\hat{A}}$). The errors as measured in standard deviations are considered most informative since they take into account the natural variability of the cells. The design objective is for the estimated α, κ and A values to consistently lie within a distance of one true standard deviation from their true values (i.e. $|\zeta_\alpha| < 1$, $|\zeta_\kappa| < 1$ and $|\zeta_A| < 1$) for all image types.

The LSEF method was accurate for estimating $\hat{\alpha}$ since $|\zeta_\alpha|$ was always less than 0.59. The LSEF method, as well the AM and CORR methods, had difficulty with image (a) and (j) since $\hat{\kappa}$ is very close to 1; meaning that the composite cell is almost circular and hence $\hat{\alpha}$ is difficult to detect, even visually. In contrast, the orientation in image (c) is easily detected because $\hat{\kappa}$ is large. For estimating $\hat{\kappa}$, the LSEF achieved the goal of $|\zeta_\kappa| < 1$ for every image. The largest errors were for images

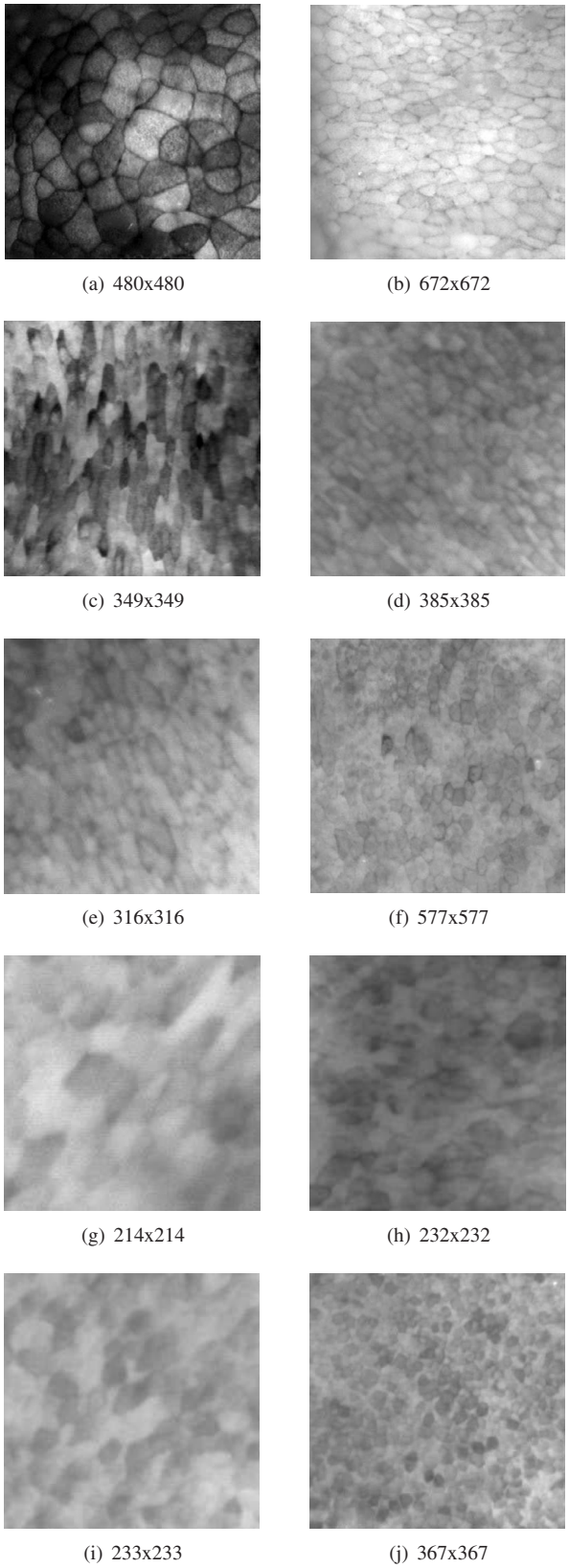

(a) 480x480 (b) 672x672 (c) 349x349 (d) 385x385 (e) 316x316 (f) 577x577 (g) 214x214 (h) 232x232 (i) 233x233 (j) 367x367

Fig. 8. Test images and image sizes in pixels.

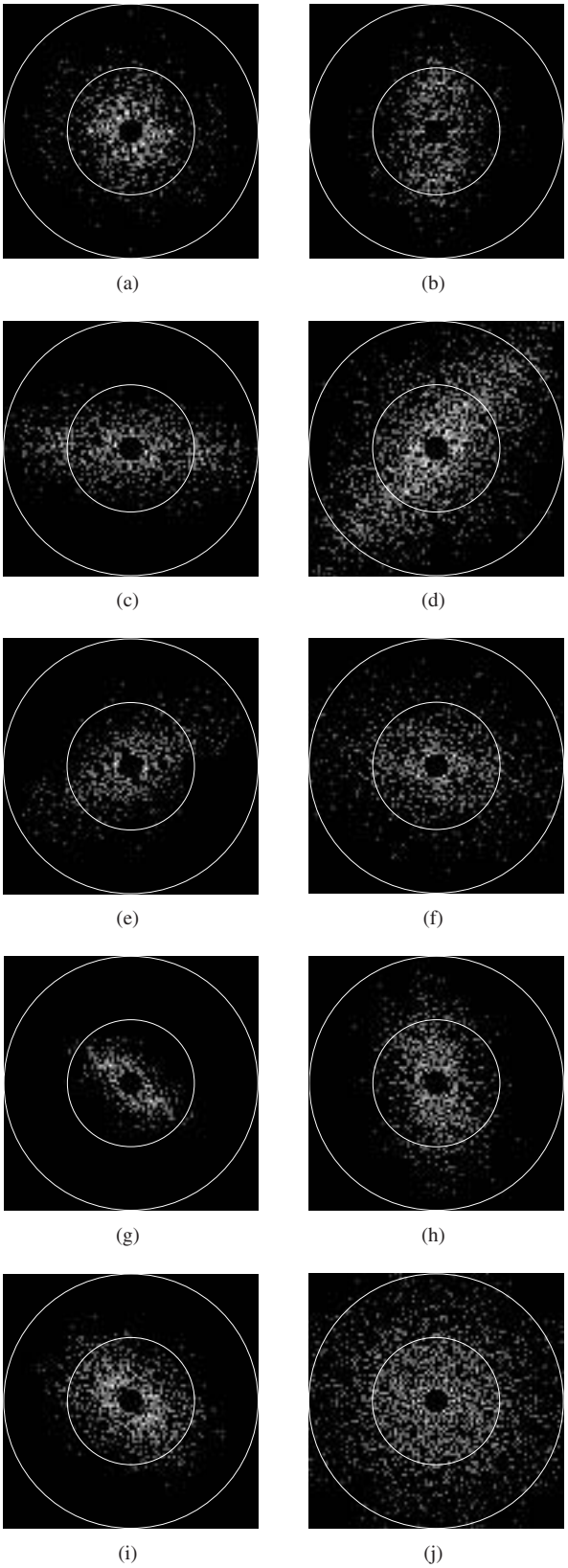

Fig. 9. $|F|$ images of test images after preprocessing. Concentric circles show 25 and 50 c.p.i.

TABLE I

DISTANCE FROM $\hat{\alpha}$ FOR EACH METHOD IN DEGREES ($\epsilon_\alpha = \alpha - \hat{\alpha}$) AND NUMBER OF STANDARD DEVIATIONS ($\zeta_\alpha = \epsilon_\alpha / \sigma_{\hat{\alpha}}$). BEST RESULTS SHOWN IN BOLD.

Image: $\hat{\alpha}$, $\sigma_{\hat{\alpha}}$	LSEF		AM		CORR	
	ϵ_α	ζ_α	ϵ_α	ζ_α	ϵ_α	ζ_α
a: 36.8°, 49.2°	+29.2°	+0.59	+21.4°	+0.43	+15.2°	**+0.31**
b:173.1°, 16.1°	-3.7°	-0.23	+1.7°	**+0.11**	+2.9°	+0.18
c: 85.9°, 17.6°	-1.1°	-0.06	+0.1°	**+0.01**	+0.1°	**+0.01**
d:141.0°, 33.1°	-3.6°	**-0.11**	-3.7°	-0.11	-5.0°	-0.15
e:120.5°, 13.3°	+1.5°	+0.11	+0.5°	**+0.04**	-3.5°	-0.26
f: 87.8°, 21.6°	-7.0°	-0.32	-7.5°	-0.35	-0.8°	**-0.04**
g: 50.0°, 8.7°	+0.5°	**+0.06**	-0.5°	**-0.06**	-1.0°	-0.11
h: 7.4°, 27.8°	+4.7°	**+0.17**	+5.0°	+0.18	+6.6°	+0.24
i: 53.3°, 35.2°	+3.1°	+0.09	+0.9°	**+0.03**	+2.7°	+0.08
j: 57.7°, 44.1°	+15.0°	+0.34	+14.3°	**+0.32**	+27.3°	+0.62
Average absolute	6.9	0.21	5.6	**0.16**	6.5	0.20

TABLE II

DISTANCE FROM $\hat{\kappa}$; FOR EACH METHOD IN DIMENSIONLESS UNITS ($\epsilon_\kappa = \kappa - \hat{\kappa}$) AND NUMBER OF STANDARD DEVIATIONS ($\zeta_\kappa = \epsilon_\kappa / \sigma_{\hat{\kappa}}$). BEST RESULTS SHOWN IN BOLD.

Image: $\hat{\kappa}$, $\sigma_{\hat{\kappa}}$	LSEF		AM		CORR	
	ϵ_κ	ζ_κ	ϵ_κ	ζ_κ	ϵ_κ	ζ_κ
a: 1.05, 0.44	+0.06	+0.14	+0.05	**+0.11**	+0.38	+0.86
b: 1.76, 0.56	-0.46	-0.82	-0.24	**-0.43**	+0.95	+1.70
c: 2.28, 0.67	-0.21	-0.31	-0.09	**-0.13**	-0.78	-1.16
d: 1.50, 0.60	+0.06	**+0.10**	+0.25	+0.42	-0.07	-0.12
e: 1.93, 0.42	-0.28	-0.67	-0.19	**-0.45**	-0.50	-1.19
f: 1.51, 0.36	-0.08	-0.22	-0.06	**-0.17**	-0.08	-0.22
g: 1.99, 0.62	-0.26	-0.42	-0.05	**-0.08**	-0.16	-0.26
h: 1.32, 0.51	+0.11	**+0.22**	+0.19	+0.37	-0.22	-0.43
i: 1.48, 0.67	-0.15	-0.22	-0.09	**-0.13**	+0.35	+0.52
j: 1.10, 0.30	-0.01	-0.03	0.00	**0.00**	+0.33	+1.10
Average absolute	0.17	0.32	0.12	**0.23**	0.38	0.76

TABLE III

DISTANCE FROM $\hat{A}$; IN SQUARE PIXELS ($\epsilon_A = A - \hat{A}$) AND NUMBER OF STANDARD DEVIATIONS ($\zeta_A = \epsilon_A / \sigma_{\hat{A}}$). BEST RESULTS SHOWN IN BOLD.

Image: $\hat{A}$, $\sigma_{\hat{A}}$	LSEF		AM		CORR	
	ϵ_A	ζ_A	ϵ_A	ζ_A	ϵ_A	ζ_A
a: 2744, 1267	-2135	-1.69	-1107	-0.87	-180	**-0.14**
b: 2027, 708	-871	-1.23	+66	**+0.09**	+624	+0.88
c: 479, 200	-206	-1.03	+161	**+0.81**	+1272	+6.36
d: 619, 222	-440	-1.98	-115	**-0.52**	+1027	+4.63
e: 656, 178	-372	-2.09	+31	**+0.17**	+450	+2.53
f: 1010, 395	-461	**-1.17**	+658	+1.67	+2700	+6.84
g: 810, 233	-504	-2.16	-244	**-1.05**	-275	-1.18
h: 337, 152	-200	-1.32	-17	**-0.11**	+41	+0.27
i: 373, 158	-219	-1.39	-29	**-0.18**	+262	+1.60
j: 194, 85	-62	**-0.73**	+160	+1.88	+1301	+15.31
Average absolute	547	1.50	258	**0.74**	811	2.08

(b) and (e), which were due to the fitted ellipse being pulled by energy in the L_{major} direction. This reveals a weakness of the LSEF method: energy responses away from the fitted ellipse have a strong effect on it due to the squared nature of the distance measure. This problem affected the LSEF estimation of $\hat{A}$: the fitted ellipse was too large for every image, resulting in a consistent underestimation of $\hat{A}$.

The AM method performed slightly superior to the LSEF method in estimating $\hat{\alpha}$ and $\hat{\kappa}$, and also achieved the goals of $|\zeta_\alpha| < 1$ and $|\zeta_\kappa| < 1$. The method also achieved $|\zeta_A| < 1$ except for images (f), (g) and (j). It was found that the threshold T_3 was appropriate for images with 10-18 minor axis cycles per image. Images (f) and (j) exceeded this range, while image (g) was below this range. It was found that this 'usable' range was even smaller when the least-squares ellipse method was tested; hence the T_3 method was chosen.

The CORR method performed in a manner comparable to the LSEF method and achieved $|\zeta_\alpha| < 1$. This method, however, had large errors in estimating $\hat{\kappa}$ for a number of the images because the $|F|$ images rarely has well-defined peaks along the the major and minor axes. This problem negatively affected the estimation of $\hat{A}$ as well.

Average computation time for each method (not including the FFT and the preprocessing steps) in Matlab® on a Pentium 4 2.4 GHz computer is as follows: LSEF, 1.07 seconds; AM, 0.83 seconds and CORR, 4.40 seconds. An implementation of each method in a low-level language such as C++ could significantly reduce these times. Since real-time implementation is not necessary, all methods have acceptable computation times.

V. Conclusions

Four computer vision methods that use a spatial-frequency approach to determine average cell shape and orientation in an image of a biological tissue have been proposed and evaluated. Three of these methods – Least-Squares Ellipse Fitting (LSEF), Correlation (CORR) and Area Moments (AM) – successfully overcame significant variations in illumination, cell pigmentation, cell shape and cell boundary visibility.

The AM method was most accurate in estimating every composite cell parameter, averaging $|\zeta_\alpha| = 0.16$, $|\zeta_\kappa| = 0.23$ and $|\zeta_A| = 0.74$. The AM method achieved the goals of $|\zeta_\alpha| < 1$, $|\zeta_\kappa| < 1$ for all tested images. The $|\zeta_A| < 1$ goal was met when a range of 10-18 minor axis cycles per image was enforced. The LSEF method performed similarly to the AM method for estimating $\hat{\alpha}$ and $\hat{\kappa}$ but consistently underestimated $\hat{A}$. The LSEF method was also affected by outliers in the $|F|$ image due to its squared distance measure. The CORR met the $|\zeta_\alpha| < 1$ goal and yielded similar orientation results as the other two methods. The CORR method performed well estimating $\hat{\kappa}$ and $\hat{A}$ only when the peaks in the power spectrum were well defined. All methods had acceptable computation times.

Due to its consistently superior performance, it is recommended that the AM method be used to estimate all the composite cell parameters: $\hat{\alpha}$, $\hat{\kappa}$ and $\hat{A}$.

References

[1] G. W. Brodland and J. Veldhuis, "Computer simulations of mitosis and interdependencies between mitosis orientation, cell shape and epithelia reshaping," *Journal of Biomechanics*, vol. 32, pp. 673–681, 2002.

[2] G. W. Brodland. (2004, November) Research homepage. [Online]. Available: http://www.civil.uwaterloo.ca/brodland/

[3] G. W. Brodland, J. Veldhuis, and D.-L. Chen, "How cell shape affects the stresses in a cell sheet," in *ASME IMECE*, Orlando FL, Nov. 5-10 2000, pp. 79–80.

[4] J. H. Veldhuis, G. W. Brodland, C. J. Wiebe, and G. J. Bootsma, "Robotic microscope system determines regional strain rates during amphibian embryo development," *Submitted to Annals of Biomedical Engineering*, Nov 1 2003.

[5] C. Wiebe and G. W. Brodland, "Tensile properties of embryonic epithelia measured using a novel instrument," *Journal of Biomechanics. In press*.

[6] G. Vaidyanathan and P. Lynch, "Texture direction analysis using edge counts," in *Proceedings of Southeastcon '89*, vol. 2, Apr 9-12 1989, pp. 733–738.

[7] A. Sourice, G. Plantier, and J.-L. Saumet, "Autocorrelation fitting for texture orientation estimation," in *Proceedings of 2003 International Conference on Image Processing*, vol. 1, Sept 14-17 2003, pp. 281–284.

[8] J. Bigün, G. Granlund, and J. Wiklund, "Multidimensional orientation estimation with applications to texture analysis and optical flow," *IEEE Transactions on Pattern Analysis and Machine Intelligence*, vol. 13, no. 8, pp. 775–790, Aug 1991.

[9] M. Kass and A. Witkin, "Analyzing oriented patterns," *Computer Vision, Graphics and Image Processing*, vol. 37, pp. 362–385, 1987.

[10] T. Matsuyama, S.-I. Miura, and M. Nagao, "Structural analysis of natural textures by fourier transformation," *Computer Vision, Graphics and Image Processing*, pp. 347–362, October 1983.

[11] H.-B. Kim and R.-H. Park, "Extracting spatial arrangement of structural textures using projection information," *Pattern Recognition*, pp. 237–245, March 1992.

[12] V. V. Starovoitov, S.-Y. Jeong, and R.-H. Park, "Texture periodicity detection: Features, properties and comparisons," *IEEE Trans. Syst., Man, Cybern. A*, no. 6, pp. 839–849, November 1998.

[13] P. Brodatz, *Textures: A Photographic Album for Artists and Designers*. Dover, 1966.

[14] P. J. W. Iles, D. A. Clausi, and G. W. Brodland, "Estimation of average cell shape from digital images of cellular surfaces," in *Proceedings of the First Canadian Conference on Computer and Robot Vision*, May 17-19 2004, pp. 273–278.

[15] H. Chen and G. W. Brodland, "Cell-level finite element studies of viscous cells in planar aggregates," *ASME Journal of Biomechanical Engineering*, vol. 122, pp. 394–401, 2000.

[16] K. R. Castleman, *Digital Image Processing*. Englewood Cliffs, NJ: Prentice Hall, 1996.

[17] A. Fitzgibbon, M. Pilu, and R. Fisher, "Direct least square fitting of ellipses," *Pattern Analysis and Machine Intelligence*, vol. 21, no. 5, pp. 476–480, 1999.

[18] S. M. Puddister, "Estimating bulk geometrical properties of cellular structures," Master's thesis, University of Waterloo, Waterloo, ON, 2003. [Online]. Available: www.systems.uwaterloo.ca/Faculty/CurrentTenured/Clausi/clausi.html

[19] R. Hibbeler, *Mechanics of Materials*, 6th ed. Prentice-Hall, New Jersey, 2005.

[20] G. W. Brodland, "A computer model for reshaping of cells in epithelia due to in-plane deformation and annealing," *Comput Methods Biomech Biomed Engin*, vol. 6, no. 2, pp. 89–98, 2003.

[21] A. Bovik, M. Clark, and W. Geisler, "Multichannel texture analysis using localized spatial features," *IEEE Trans. Pattern Analysis and Machine Intelligence*, vol. 12, no. 1, pp. 55–73, 1990.

[22] D. A. Clausi and M. E. Jernigan, "Designing Gabor filters for optimal texture separability," *Pattern Recognition*, vol. 33, pp. 1835–1849, 2000.